

STATISTICAL STUDY OF FREE MAGNETIC ENERGY AND FLARE PRODUCTIVITY OF SOLAR ACTIVE REGIONS

J.T. Su^{1,2,3}, J. Jing¹, S. Wang^{1,2}, T. Wiegmann⁴ and H.M. Wang¹

1. Space Weather Research Laboratory, New Jersey Institute of Technology, University Heights, Newark, NJ 07102-1982, USA
2. Key Laboratory of Solar Activity, National Astronomical Observatories, Chinese Academy of Sciences, Beijing 100012, China
3. State Key Laboratory of Space Weather, Chinese Academy of Sciences, Beijing 100190
4. Max-Planck-Institut für Sonnensystemforschung, Max-Planck-Strasse 2, 37191 Katlenburg-Lindau, Germany

sjt@bao.ac.cn

Received _____; accepted _____

Not to appear in Nonlearned J., 45.

ABSTRACT

Photospheric vector magnetograms from Helioseismic and Magnetic Imager on board the Solar Dynamic Observatory are utilized as the boundary conditions to extrapolate both non-linear force-free and potential magnetic fields in solar corona. Based on the extrapolations, we are able to determine the free magnetic energy (FME) stored in active regions (ARs). Over 3000 vector magnetograms in 61 ARs were analyzed. We compare FME with ARs' flare index (FI) and find that there is a weak correlation ($< 60\%$) between FME and FI. FME shows slightly improved flare predictability relative to total unsigned magnetic flux of ARs in the following two aspects: (1) the flare productivity predicted by FME is higher than that predicted by magnetic flux and (2) the correlation between FI and FME is higher than that between FI and magnetic flux. However, this improvement is not significant enough to make a substantial difference in time-accumulated FI, rather than individual flare, predictions.

Subject headings: Sun: activity — Sun: flares — Sun: magnetic fields

1. INTRODUCTION

Solar flares are sudden brightening observed over the Sun’s surface or above the solar limb. The energy release in a flare varies from 10^{29} ergs in a sub-flare to 10^{32} ergs in a typical large event (Priest 1984). It could be up to 10^{34} ergs in the largest events such as the one on 4 November 2003 (Kane et al. 2004). The source of its energy is generally believed coming from the magnetic energy, $E = \frac{1}{8\pi} \int B(\mathbf{r}, t)^2 dV$, stored primarily in active regions (ARs). This energy has a minimum when the coronal electric current vanishes (potential field configuration), and increases in value when the field becomes twisted or open (Aly 1990). The development of flaring conditions does not depend on the total magnetic flux, but depends on the availability of free magnetic energy (FME) and the triggering processes to release it (Low 1982). The FME in magnetic field is the amount of magnetic energy in excess of the minimum energy attributed to the potential field $\mathbf{B}(\mathbf{r}, t)^p$ (Sturrock 1967). It can be roughly estimated from vector magnetograph data on the photosphere with the Virial expression (Molodensky 1974)

$$E_{free} = \frac{1}{4\pi} \int \int B_z [x(B_x - B_x^p) + y(B_y - B_y^p)] dx dy, \quad (1)$$

where $\mathbf{B}(\mathbf{r}, t)$ is assumed to be force-free and vanishes when $(x^2 + y^2 + z^2)^{1/2} \rightarrow \infty$. The formula can also be extended with the Virial theorem to the case in which the field is not force-free but in a static equilibrium with plasma pressure and gravity (Low 1982). In the latter case, the total energy of the system contains not only the magnetic energy, but also thermal and gravitational energy. In general, when using Eq. (1) to estimate FME, it is hard to estimate errors that would be introduced in the calculations, as the fields are neglected in the lateral and upper boundaries.

At present, exact measurements of the three dimensional (3-D) fields are not yet available and vector magnetic fields are only measured in the photospheric level. Methods using magnetically sensitive coronal spectral lines (Judge et al. 2013) or coronal seismology

(Van Doorsselaere et al. 2007) have been developed. These methods, however, do not provide a quantitative 3-D structure of the coronal fields. With the observed photospheric vector magnetic fields, there are several ways to obtain the 3-D magnetic field in the corona. One of them is the data-driven magnetohydrodynamics (MHD) modeling (Wu et al. 2006). This approach, although more computationally intensive and less routinely used, gives impressive results in recent studies (Jiang et al. 2012; Fan et al. 2011). Another useful approach is the well-known nonlinear force-free (NLFF) field extrapolation, using the vector photospheric magnetograms as the boundary condition (Wiegelmann 2004; Schrijver et al. 2008; De Rosa et al. 2009). With a NLFF field, FME may be evaluated by the expression

$$E_{1free} = \frac{1}{8\pi} \int (B^2 - B^{p2})dV, \quad (2)$$

which has been used in many recent studies (e.g., Jing et al. 2010; Gilchrist et al. 2012).

Similarly, there is another expression to evaluate FME

$$E_{2free} = \frac{1}{8\pi} \int (\mathbf{B} - \mathbf{B}^p)^2 dV, \quad (3)$$

where $\mathbf{B} - \mathbf{B}^p$ is called the source field to describe the nonpotentiality of the magnetic field (Hagyard et al. 1981; Wang et al. 1996). In general, Eq. (2) gives the energy difference between the NLFF field \mathbf{B} and the respective potential field \mathbf{B}^p , while Eq. (3) gives the total energy of the non-potential field $\mathbf{B} - \mathbf{B}^p$. Their difference, over the entire volume V , amounts to zero, given the well-known decomposition of the non-potential field \mathbf{B} into poloidal \mathbf{B}^p and toroidal $\mathbf{B} - \mathbf{B}^p$ components. Using the above two equations, we may define a mean value to estimate FME, namely

$$E_{3free} = \frac{1}{2}(E_{1free} + E_{2free}), \quad (4)$$

with uncertainty

$$\Delta E_{free} = \frac{1}{4\pi} \int |\mathbf{B}^p \cdot (\mathbf{B}^p - \mathbf{B})| dV, \quad (5)$$

which is derived from Eq.(2)-Eq.(3). The magnetic field measurements and errors in extrapolation contribute to this uncertainty. In addition, E_{free} determined with Eq.(4) is regarded as the upper limit of the energy that is available to power flares/CMEs because not all of the FME mentioned above is free. Constrained by the conservation of total magnetic helicity, the lowest energy state of ARs is actually linear force free (LFF) field instead of potential field (Woltjer 1958; Taylor 1974, 1976). In this case, the FME should be estimated by $E_{free} = E - E_{lff}$, the difference between the total energy and the energy of a LFF field. However, LFF fields are unrealistic for the open upper halfspace, because the energy is unbounded (see Seehafer 1978). Thus, one often finds E_{free} from the difference $E - E_{lff}$ being negative.

In the past three decades, as the diagnosis of magnetic fields in the chromosphere and corona is difficult, various surface nonpotentiality indices of the solar ARs have been developed to predict flares (see Leka & Barnes 2003; Yang et al. 2012), such as magnetic shear angle (e.g., Hagyard et al. 1984; Ambastha et al. 1993; Wang et al. 1994; Li et al. 2000; Tian et al. 2002), electric current (e.g., Canfield et al. 1993; Leka 1999; Wang et al. 1996; Zhang 2001), current helicity (e.g., Seehafer 1990; Bao et al. 1999), subsurface kinetic helicity (Gao et al. 2012, 2014), horizontal magnetic gradient (e.g., McIntosh 1990; Zirin & Wang 1993; Zhang et al. 1994; Tian et al. 2002; Cui et al. 2006), length of the high-gradient and high-sheared polarity inversion line (Falconer et al. 2003; Schrijver et al. 2005; Cui et al. 2006; Jing et al. 2006), effective distance between two opposite magnetic polarities in one AR (Chumak et al. 2004; Guo et al. 2006) and photospheric excess energy (Wang et al. 1996; Metcalf et al. 1995; Moon et al. 2002; Leka & Barnes 2003). Compared with those photospheric nonpotentiality indices, FME derived from 3-D coronal magnetic configuration over ARs seems to be a more direct physical parameter related to the available energy to power flares. Based on 75 AR's magnetograms, Jing et al. (2010) conducted a pilot study of the statistical correlation between FME derived from 3-D NLFF

fields and flare index (FI) (Antalova 1996; Abramenko 2005). They found a positive correlation between the FME and flare productivity of solar ARs. In this study, we revisit this issue by using a much more extended sample of AR vector magnetograms obtained with SDO/HMI. We study both FME and total unsigned magnetic flux (Φ) of ARs in order to compare their respective abilities to predict flare productivity. In addition, we explore the statistical correlation between FI and other magnetic parameters: the total unsigned electric current $I_t = \int |J_z| ds = \frac{1}{4\pi} \int |\partial B_y / \partial x - \partial B_x / \partial y| ds$ (Canfield et al. 1993; Leka 1999), the averaged twisted measure $\alpha_{av} = \sum J_z(x, y) \text{sign}[B_z(x, y)] / \sum |B_z(x, y)|$ (Hagino & Sakurai 2004), and the proxy of photospheric excess energy $E_{pe} = \frac{1}{8\pi} \int (\mathbf{B} - \mathbf{B}^p)^2 ds$. Table 1 lists all the parameters investigated in this paper.

2. DATA REDUCTION

The data sample includes 6261 photospheric vector magnetograms covering 61 ARs. The center locations of these magnetograms are within 45-degree from the disk center, and their disk passage is in the period of May 2010 through April 2013 as listed in Table 2. The magnetograms are obtained with the Helioseismic and Magnetic Imager (HMI) on board the Solar Dynamics Observatory (SDO). We use the SHARP (Spaceweather HMI Active Region Patches) data series (Turmon et al. 2010) which are re-mapped in Cartesian coordinates using Cylindrical Equal Area (CEA) projection. The 180-degree ambiguity in the transverse field has been resolved with Metcalf’s Minimum Energy method (Leka et al. 2009). The resolution of the original magnetogram data is about $0.''5 \text{ pixel}^{-1}$. To speed up extrapolation, we lower the resolution and rebin them to $3'' \text{ pixel}^{-1}$. We preprocess the photospheric magnetograms using a method devised by Wiegmann, Inhester & Sakurai (2006). NLFF fields and potential fields are then extrapolated from the preprocessed photospheric boundary with the weighted optimization (Wiegmann 2004) and FFT

(Seehafer 1978) methods, respectively.

Note that we do not include smoothing in the data preprocessing. To investigate how the results vary due to the smoothing, we carry out some testing extrapolations. Two sets of vector magnetograms are used as the bottom boundary of the NLFF field extrapolation: the magnetograms smoothed over a $3'' \times 3''$ area, and the same magnetograms without smoothing. The magnetograms used here were taken in AR 11158 spanning from 00:00 UT of 2011 February 12 to 15:48 UT of February 15 with a cadence of 12 min. Figure 1(a) shows E_{3free}^s (with smoothing) versus E_{3free}^{ns} (without smoothing). The blue line is a linear fitting to the data. The smoothed results seem to diverge for $E_{3free}^s > 4 \times 10^{32}$ ergs, but below this limit they give very similar FME values to those obtained without smoothing. Even so, the rank correlation coefficient (RCC), which assesses how well the relationship between two variables and can be described using a monotonic function, is very high up to 93%. We give the correlation's confidence level defined as $(1 - P_s) \times 100\%$ shown in parentheses in the bottom right corner of panels (a) and (c), where P_s is the probability (binomial distribution) that the observed correlation would occur by random chance. It is calculated by the routine *erfcc* described in section 14.6 of Numerical Recipes (Press et al. 1992). We also evaluate the variation of FMEs from the magnetograms in different spatial resolution. The data of AR 11158 at 19:48:00 UT on 2011 February 13 is used. The obtained values are 1.84×10^{32} , 1.89×10^{32} and 1.64×10^{32} ergs, corresponding to the spatial resolutions of, $1.5''$, $2.0''$ and $3.0''$, respectively. Therefore, FME does not change significantly with different resolutions, so it would not affect our conclusion.

Now we consider the magnetic flux imbalance in our data sample. It may be evaluated by the ratio of the net flux to the total unsigned one in the field of view, $r_{im} = |\sum B_z ds| / \sum |B_z| ds$. A histogram of r_{im} for all the data is shown in Figure 1(b). It is found that except for some data with a very large r_{im} (e.g. 0.6), most of the data

(> 76%) shows a value of r_{im} less than 0.2.

After these procedures, we obtain all the extrapolated 3-D fields based on 6261 vector magnetograms. E_{1free} and E_{2free} from Eqs. (2) and (3) are then determined subsequently. Figure 1(c) shows a scatter plot of E_{1free} versus E_{2free} for all the data. Their correlation is very high, up to $\sim 93\%$. A linear fit (blue line) shows that E_{2free} is greater than E_{1free} with a factor ~ 1.1 . Their difference (see Eq. (5)) can be used to evaluate the uncertainty of E_{3free} . For our case, however, the relative error may be more helpful. Therefore, we define a relative one of E_{3free} , namely $r_{un} = \Delta E_{free}/E_{3free}$, whose histogram is shown in Figure 1(d). We find that $\sim 71\%$ of FMEs is with $r_{un} \leq 0.3$. To further ensure the reliability of the analysis, we exclude both samples, those with the flux imbalance $r_{im} > 0.2$ and those with the relative FME uncertainty $r_{un} > 0.3$. Finally, the remained sample of 3226 vector magnetograms are used for further analysis.

3. ANALYSIS AND RESULTS

3.1. DEFINITION OF FLARE INDEX

Solar flares are conventionally classified as X, M, C, or B according to their peak soft X-ray (SXR) flux in the wavelength range 1 to 8 Angstroms, as measured by the Geostationary Operational Environmental Satellite (GOES) and recorded in the NOAA Space Environment Center’s solar event reports. The peak flux of X-, M-, C- and B-class flares is of 10^{-4} , 10^{-5} , 10^{-6} and 10^{-7} W m $^{-2}$ magnitude order, respectively. If given the beginning and ending time of a time window, then the dimensionless FI in this interval τ (usually measured in days) is defined as

$$FI = (100 \times \sum_{\tau} I_X + 10 \times \sum_{\tau} I_M + 1 \times \sum_{\tau} I_C + 0.1 \times \sum_{\tau} I_B) / I_{C1.0}, \quad (6)$$

where I_X , I_M , I_C , and I_B are the SXR peak flux of X-, M-, C-, and B-class flares, respectively, produced by one AR within τ -days. This definition measures a time-accumulated flare production, which is somehow different from the time-averaged flare production used in Antalova (1996) and Abramenko (2005). When we study the correlation between FME and flare production in a fixed time period, there is no difference between the time-accumulated FI used here and the time-averaged FI used in previous studies. However, they are different when we study the frequency distributions and the power-law indices of flare production (Subsection 3.2). Thereafter, the abbreviation of FI in this paper refers to the time-accumulated flare index. Moreover, to characterize the ARs with certain flare magnitudes, we set a series of thresholds of FI to study their correlations with the magnetic parameters of ARs. For example, if we investigate the $\geq C1.0$, $\geq M1.0$ and $\geq M5.0$ flare productions, then will set $FI \geq 1$, 10 and 50, respectively. Accordingly, $FI \geq 0$ denotes all the ARs' data satisfying this condition, no matter whether the ARs are flare productive or not.

3.2. POWER-LAW DISTRIBUTION OF FME AND FI

Statistical analyses show that most of the frequency distributions of parameters related to solar activities can be characterized by power-law distributions (Aschwanden 2011), which reflects an underlying power law in the distribution of energy release (Akabane 1956; Hudson 1991; Wheatland 2000). We also find such a distribution in the histograms of FME, FI and magnetic flux shown in Figure 2. The histograms use all the data identified by $FI \geq 0$. We apply chi-square (χ^2) test to evaluate whether they obey power-law distribution $N(S) \sim S^{-\alpha}$ or not, where S refers to E_{3free} , FI and Φ , and α is the power-law index. The FME and FI data are divided into 10 bins, and those of magnetic flux, 15 bins. Figure 2(b) shows that one of the bins in the histogram (350 ~ 600) of FI_{1-day} has the

sample size $N < 5$, so the χ^2 -test cannot be applied to this histogram. The test to the other histograms shows that the values of α are ~ 2 and 1.8 for the FME and magnetic flux distribution, respectively, and ~ 1.5 for FI in the time window of 2- or 3-days, which are comparable to the index of total energy release in soft X-ray (1.5-1.6), and that of the peak flux (1.7) (Song et al. 2012).

Table 3 lists the values of α when the thresholds of FI are set as $FI \geq 0, 1, 10$ and 50 in the time windows $\tau = 1 - 3$ days. The power-law index 1.4 – 1.5 of FI does not change much with the increasing thresholds, whereas that of E_{3free} decreases systematically from ~ 2 to 1.5. The index of magnetic flux also shows a decrease, but with a large fluctuation. Generally, in most cases the difference between the power-law indices, of FI, FME, and the flux is insignificant, that is within measurement/fitting errors.

3.3. FLARING PRODUCTIVITY AT DIFFERENT THRESHOLD OF FI

We set 5 thresholds for FI, namely $FI \geq 0, 1, 10, 50$ and 100. The histograms of E_{3free} and Φ under these thresholds are shown in the first row of Figures 3 and 4, respectively. We here introduce the definition of flare productivity $P(X) = S_a(X)/S_t(X)$ (Cui et al. 2006), where X is of one measure describing magnetic properties, $S_a(X)$ and $S_t(X)$ are the number of events (their flaring activity independent of strength) and the total samples, respectively. It denotes flaring productivity of the ARs under certain properties of nonpotentiality and magnetic flux. With this definition, $P(E_{3free})$ and $P(\Phi)$ are obtained at different thresholds of FI , as illustrated in the second row of Figure 3 and 4, respectively. In these panels, the black solid lines are the Boltzmann sigmoidal fittings (Cui et al. 2006) to the curves of flare productivity. In the top panels of Figure 3, we notice that the data show discontinuity in the energy range of $8.5 - 12.3 \times 10^{32}$ ergs with a bump appearing at the position of 12.3×10^{32} ergs. We thus plot a dotted-line crossing the blue-line bump ($\geq M1.0$ flares)

in the first panel of Figure 3, which roughly corresponds to the sample number of 50. Therefore, in order to guarantee statistical significance, we do not fit the flare productivity when $S_t(X)$ is less than 50.

We attempt to further illustrate the flare productivity predicted by E_{3free} and Φ with a specific case. For instance, when the FME is taken at 5.0×10^{32} ergs, roughly corresponding to the magnetic flux at 3.0×10^{22} Mx (see Figure 7(a)), the corresponding flare productivity within the time windows of $\tau = 1 - 3$ days can be obtained as listed in Table 4. Generally, P declines rapidly with increasing threshold and rises steadily with the increase of the time window. Moreover, P is higher as predicted by E_{3free} in each time window at a given threshold, suggesting that this parameter can give a slightly better prediction for FI than Φ . In addition, we cannot give the productivity when $E_{3free} > 8 \times 10^{32}$ ergs, as the sample size is inadequate ($N < 50$). It indicates that more AR samples that produce large flares ($>M5.0$) are needed to supplement this study to make a more accurate flare forecasting for larger events.

3.4. CORRELATION OF FI WITH FME/MAGNETIC FLUX

Figure 5 shows the scatter plots of E_{3free} versus FI (top) and Φ versus FI (bottom) for all the data ($FI \geq 0$), respectively. In spite of the fact that the data are widely scattered, the results still reveal a weak positive correlation between the quantities. For instance, in $\tau = 2$ -days the RCC between E_{3free} and FI is 57% and the RCC between Φ and FI 55%. Generally, the correlations of FI with E_{3free} and Φ are nearly equivalent in the selected time windows, which are comparable to, but less than, the 65% correlation between eruptive-flare production and AR sigmoidality as well as size (Canfield et al. 1999).

Furthermore, Figure 6 shows that the RCC varies with the thresholds of FI (panels (a)

and (b)), FME (panel (c)) and magnetic flux (panel (d)). For convenience, we define here the threshold of FI as TFI. The relationship between them, e.g. $FI \geq 0, 1, \dots$ is equivalent to $TFI = 0, 1, \dots$. Likewise, the threshold of FME is defined as TFME and that of magnetic flux as TMF. In the figure, the maximum of TFI is set to be 50 (at this threshold $N = 528$), that of $TFME$ is 1.3×10^{33} ergs ($N = 50$), and that of TMF is 5.0×10^{22} Mx ($N = 106$). Panels (a) and (b) respectively show the RCC between FME and FI and RCC between magnetic flux and FI as a function of TFI . Both RCCs change with a very similar trend: declining first when $TFI < 10$, then rising at larger threshold ($10 < TFI < 26$), and finally keeping nearly unchanged when $TFI > 26$. Note that the variation of the RCCs in the range of $10 < TFI < 26$ is opposite to that of $TFI < 10$, increasing with the decreasing time window. A similar feature can be found in Figure 6(d) for the correlation between Φ and FI , and the turnover point occurs at $\sim TMF = 1.9 \times 10^{22}$ Mx. In Figure 6(c) for the correlation between E_{3free} and FI , the RCCs exhibit a large fluctuation with $TFME$. Those in the 2- and 3-day time windows change similarly in magnitude, but are all greater than that in the 1-day time window. A remarkable feature is that the RCCs decrease first when the threshold is less than $\sim 2.9 \times 10^{32}$ ergs, while then increase when it is greater than $\sim 6.5 \times 10^{32}$ ergs. However, in Figure 6(d) the RCCs only show a monotonically decreasing trend in the entire range of TMF . This reflects that ARs with the larger FME, rather magnetic flux, are more favorable to produce flares (Low 1982).

Figure 7 shows the scatter plots of Φ versus E_{3free} (panel(a)), I_t (panel (b)), E_{pe} (panel (c)) and α_{av} (panel (d)) for all the data ($FI \geq 0$), respectively. Except α_{av} , the correlations of Φ with the others are very high, more than 90%. We note that there are likely two slopes in the $E_{3free} - \Phi$ plot with the turning point occurs at $\sim \Phi = 3 \times 10^{21}$ Mx. Similarly, we can find this feature in Figure 5(a) of Jing et al. (2010). Finally, we list the RCCs of FI/Φ with all the used measures in Table 5. Generally, the RCCs associated with FI are relatively weak ($\leq 65\%$), and those with Φ are very strong ($\geq 90\%$) except the measure of

twist. This confirms reports that there is no discernible correlation between the magnetic twist measure and magnetic flux (Falconer et al. 2006).

4. SUMMARY AND DISCUSSION

In this paper, based on a data sample of 3226 vector magnetograms in 61 active regions, we present the frequency distributions of free magnetic energy (FME) (i.e., E_{3free} defined in Eq. (4)), flare index (FI), and total unsigned magnetic flux (Φ). We also analyze the potential of E_{3free} and Φ as flare predictors and examine the magnitude scaling correlation between FI and several magnetic measures such as E_{3free} , Φ , total unsigned electric current I_t , proxy of photospheric free magnetic energy E_{pe} and averaged magnetic twist measure α_{av} .

It is found that the frequency functions of FME, FI and magnetic flux all exhibit a power-law distribution. The index of E_{3free} (see Table 3), which is steeper than that of FI (Φ), varies from the maximum 2.0 to ~ 1.5 with the threshold of FI . The difference between the power-law indices, of FI, FME, and the flux is insignificant. We also find that E_{3free} shows an improved flare predictability (demonstrated in Table 4) in comparison with Φ . However, in terms of the magnitude scaling correlation between $FI_{\tau-day}$ and E_{3free} , Φ , I_t , E_{pe} and α_{av} (see Table 5) based on all the used samples, the magnetic measure of FME shows no improvement for flare predictability. This result is consistent with the previous study of Jing et al. (2010). We then set a series of thresholds for FI , E_{3free} and Φ to study how the above correlations vary with these thresholds. It is found that the correlation between Φ and FI shows a general decreasing trend with an increasing threshold of flux, while that between E_{3free} and FI increases when the threshold of FME is greater than 6.5×10^{32} ergs. This suggests that ARs with the larger FME rather magnetic flux are more favorable to produce flares (Low 1982).

Generally speaking, despite the fact that E_{3free} is one of the most direct measures of the available energy in a 3-D magnetic field, our large-sample study shows that its correlation with $FI_{\tau-day}$ is still weak ($< 60\%$). Jing et al. (2010) gave a detailed discussion about the cause of the lack of satisfactory results, such as the quality of the extrapolated NLFF fields which is influenced by a number of inadequacies of the boundary data, uncertainties in the data reduction, etc. In the present study, we first evaluate the flux imbalance in our chosen sample as shown in Figure 2(b) and find that most of the data ($> 76\%$) are of with $r_{im} < 0.2$. We then evaluate the uncertainty in the determined FME and find $\sim 71\%$ of the sample with $r_{un} < 0.3$ as shown in Figure 1(d). To ensure the reliability of the analysis, these two types of data are excluded from the original sample.

We also evaluated the energy in excess of the LFF component $E_{free} = E - E_{lff}$ with the averaged twisted measure α_{av} (Hagino & Sakurai 2004), and found E_{free} of nearly half of all the data is negative. These negative values hamper us to give a further analysis. One way to get around this problem is to find the relative magnetic helicity from the extrapolated NLFF field and infer the constant α -value corresponding to this helicity, then further calculate a LFF field and its corresponding E_{lff} . However, this is beyond the scope of the current paper.

The authors thank the anonymous referee for helpful suggestions and comments on the manuscript, which significantly improve the work. This work is supported by the Grants: National Basic Research Program of China under grant 2011CB8114001, the Specialized Research Fund for State Key Laboratories, the Key Laboratory of Solar Activity of CAS (KLSA201313), 11373040, KJCX2-EW-T07, 11178005, 11221063 and 11203036. JJ and HW are supported by US NASA grant NNX11AQ55G and NSF grants AGS 1153226, AGS 1153424 and AGS 1250374.

REFERENCES

- Abramenko, V.I. 2005, ApJ, 629, 1141
- Akabane, K. 1956, PASJ, 8, 173
- Aly, J.J. 1990, Physics of Fluids B, 2, 1928
- Ambastha, A., Hagyard, M. J., & West, E. A. 1993, Sol. Phys., 148, 277
- Antalova, A. 1996, Contributions of the Astronomical Observatory Skalnaté Pleso, 26, 98
- Aschwanden, M.J. 2011, Self-Organized Criticality in Astrophysics, by Markus J. Aschwanden. Springer-Praxis, Berlin ISBN 978-3-642-15000-5, 416p.
- Bao, S.D., Zhang, H.Q., Ai, G.X., & Zhang, M. 1999, A&AS, 139, 311
- Barnes, G., & Leka, K. D. 2008, ApJ, 688, L107
- Canfield, R.C., de La Beaujardiere, J.F., Fan, Y., et al. 1993, ApJ, 411, 362
- Canfield, R.C., Hudson, H.S., & McKenzie, D.E. 1999, Geophys. Res. Lett., 26, 627
- Chae, J., Moon, Y.J., & Park, Y.D. 2004, Sol. Phys., 223, 39
- Chumak, O., Zhang, H., & Gou, J. 2004, Astronomical and Astrophysical Transactions, 23, 525
- Cui, Y.M., Li, R., Zhang, L.Y., He, Y.L., & Wang, H.N. 2006, Sol. Phys., 237, 45
- De Rosa, M. L., Schrijver, C. J., Barnes, G., et al. 2009, ApJ, 696, 1780
- Falconer, D. A., Moore, R. L., & Gary, G. A. 2003, J. Geophys. Res.(Space Phys.), 108, 1380
- Falconer, D.A., Moore, R.L., & Gary, G.A. 2006, ApJ, 644, 1258

- Fan, Y. L., Wang, H. N., He, H., & Zhu, X. S. 2011, *ApJ*, 737, 39
- Gao, Y., Zhao, J., & Zhang, H. 2012, *ApJ*, 761, L9
- Gao, Y., Zhao, J., & Zhang, H. 2014, *Sol. Phys.*, 289, 493
- Gilchrist, S.A., Wheatland, M.S., & Leka, K.D. 2012, *Sol. Phys.*, 276, 133
- Guo, J., Zhang, H., Chumak, O. V., & Liu, Y. 2006, *Sol. Phys.*, 237, 25
- Hagino, M., & Sakurai, T. 2004, *PASJ*, 56, 831
- Hagyard, M., Low, B.C., & Tandberg-Hanssen, E. 1981, *Sol. Phys.*, 73, 257
- Hagyard, M.J., Teuber, D., West, E.A., & Smith, J.B. 1984, *Sol. Phys.*, 91, 115
- Hudson, H.S. 1991, *Sol. Phys.*, 133, 357
- Jing, J., Song, H., Abramenko, V., Tan, C., & Wang, H. 2006, *ApJ*, 644, 1273
- Jing, J., Tan, C., Yuan, Y., et al. 2010, *ApJ*, 713, 440
- Jiang, C., Feng, X., Wu, S. T., & Hu, Q. 2012, *ApJ*, 759, 85
- Judge, P.G., Habbal, S., & Landi, E. 2013, *Sol. Phys.*, 161
- Leka, K. D. 1999, *Sol. Phys.*, 188, 21
- Leka, K. D., & Barnes, G. 2003, *ApJ*, 595, 1277
- Leka, K.D., Barnes, G., Crouch, A.D., et al. 2009, *Sol. Phys.*, 260, 83
- Li, H., Sakurai, T., Ichimoto, K., & UeNo, S. 2000a, *PASJ*, 52, 465
- Low, B.C. 1982, *Sol. Phys.*, 77, 43
- Kane, S. R., McTiernan, J. M., & Hurley, K. 2005, *Å*, 433, 1133

- McIntosh, P. S. 1990, *Sol. Phys.*, 125, 251
- Metcalf, T. R., Litao, J., McClymont, A. N., Canfield, R. C., & Uitenbroek, H. 1995, *ApJ*, 439, 474
- Molodensky, M.M. 1974, *Sol. Phys.*, 39, 393
- Moon, Y.J., Choe, G. S., Yun, H. S., Park, Y. D., & Mickey, D. L. 2002, *ApJ*, 568, 422
- Parnell, C.E., DeForest, C.E., Hagenaar, H.J., et al. 2009, *ApJ*, 698, 75
- Press, W. H., Teukolsky, S. A., Vetterling, W. T., & Flannery, B. P. 1992, Cambridge: University Press, c1992, 2nd ed.
- Priest, E.R. 1984, *Solar Magnetohydrodynamics*, D. Reidel Publishing Company
- Priest, E.R., & Forbes, T.G. 2002, *A&A Rev.*, 10, 313
- Schrijver, C.J., De Rosa, M.L., Title, A. M., & Metcalf, T.R. 2005, *ApJ*, 628, 501
- Schrijver, C. J., De Rosa, M. L., Metcalf, T., et al. 2008, *ApJ*, 675, 1637
- Seehafer, N. 1978, *Sol. Phys.*, 58, 215
- Seehafer, N. 1990, *Sol. Phys.*, 125, 219
- Song, Q., Huang, G., & Tan, B. 2012, *ApJ*, 750, 160
- Sturrock, P.A. 1967, in P. A. Sturrock (ed.), *Plasma Astrophysics*, Academic Press, P.168
- Taylor, J.B. 1974, *Phys. Rev. Letters*, 33, 1139
- Taylor, J.B. 1976, in D. E. Evans (ed.), *Pulsed High Beta Plasmas*, Pergamon Press, Oxford, p.59
- Tian, L., Wang, J., & Wu, D. 2002, *Sol. Phys.*, 209, 375

- Turmon, M., Jones, H. P., Malanushenko, O. V., & Pap, J. M. 2010, *Sol. Phys.*, 262, 277
- Van Doorselaere, T., Nakariakov, V.M., & Verwichte, E. 2007, *A&A*, 473, 959
- Wang, H., Ewell, M. W., Jr., Zirin, H., & Ai, G. 1994, *ApJ*, 424, 436
- Wang, J., Shi, Z., Wang, H., & Lue, Y. 1996, *ApJ*, 456, 861
- Wheatland, M.S. 2000, *ApJ*, 532, 1209
- Wiegelmann, T. 2004, *Sol. Phys.*, 219, 87
- Wu, S. T., Wang, A. H., Liu, Y., & Hoeksema, J. T. 2006, *ApJ*, 652, 800
- Wang, A. H., Wu, S. T., Liu, Y., & Hathaway, D. 2008, *ApJ*, 674, L57
- Woltjer, L. 1958, *Proceedings of the National Academy of Science*, 44, 489
- Yang, X., Zhang, H.Q., Gao, Y., Guo, J. & Lin, G.H., 2012, *Sol. Phys.*,
- Zhang, H. 2001, *ApJ*, 557, L71
- Zhang, H., Zi, G., Yan, X., Li, W., & Liu, Y. 1994, *ApJ*, 423, 828
- Zirin, H., & Wang, H. 1993, *Sol. Phys.*, 144, 37

Table 1: Definitions of the physical parameters used in the paper.

Index	Description	Variable	Formula
1	Free Magnetic energy ¹	E_{1free}	$\frac{1}{8\pi} \int (B^2 - B^p)^2 dV$
2	Free Magnetic energy ²	E_{2free}	$\frac{1}{8\pi} \int (\mathbf{B} - \mathbf{B}^p)^2 dV$
3	Free Magnetic energy ³	E_{3free}	$\frac{1}{2}(E_{1free} + E_{2free})$
4	Relative energy error	r_{un}	$\frac{1}{4\pi} \int \mathbf{B}^p \cdot (\mathbf{B}^p - \mathbf{B}) dV / E_{3free}$
5	Total unsigned flux	Φ	$\int \mathbf{B} \cdot d\mathbf{S}$
6	Flux imbalance	r_{im}	$ \int B_z ds / \int B_z ds$
7	Total unsigned current	I_t	$\frac{1}{4\pi} \int \partial B_y / \partial x - \partial B_x / \partial y ds$
8	Proxy of free energy	E_{pe}	$\frac{1}{8\pi} \int (\mathbf{B} - \mathbf{B}^p)^2 ds$
9	Averaged twist measure	α_{av} ^a	$\sum J_z(x, y) \text{sign}[B_z(x, y)] / \sum B_z(x, y) $
10	Flare index	FI	$(100 \sum_{\tau} I_X + 10 \sum_{\tau} I_M + 1 \sum_{\tau} I_C + 0.1 \sum_{\tau} I_B) / I_{C1.0}$

^aIt is calculated following that of Hagino & Sakurai (2004).

Table 2. Information of 61 chosen ARs

NO.	AR	Date	Frames	Maxi ^a Flare	Loc	Begin ^b (UT)	End (UT)	Volume (Mm ³)
1	11072	10/05/20-26 ^c	144	B6.5	S16W32	15:46 (25)	15:55	183×183×174
2	11084	10/07/02	24	183×183×174
3	11093	10/08/07	5	M1.0	N12E31	18:24	18:47	305×192×174
4	11112	10/10/16	24	M2.9	S19W29	19:07	19:15	174×157×174
5	11158	11/02/12-16	12	X2.2	S21W21	01:44 (15)	02:06	218×218×174
6	11164	11/03/01-06	146	C8.6	N20W39	14:41 (06)	14:47	261×235×174
7	11165	11/03/01-02	48	174×130×174
8	11166	11/03/06-10	120	X2.2	N08W05	23:13 (09)	23:29	218×218×174
9	11169	11/03/09-14	133	C5.0	N21E22	20:56 (09)	21:25	261×148×174
10	11283	11/09/03-08	120	X2.1	N14W18	22:12 (06)	22:24	218×182×174
11	11287	11/09/08-11	95	261×235×174
12	11289	11/09/09-11	53	C1.7	N22E26	17:21 (10)	17:31	261×157×174
13	11302	11/09/25-28	71	M4.0	N13E35	05:06 (26)	05:13	261×183×174
14	11305	11/09/28-30	54	M1.0	N08E06	18:55 (30)	19:15	253×130×174
15	11339	11/11/05-11	36	M1.8	N21E34	20:31 (06)	20:54	261×235×174
16	11346	11/11/15	24	M1.9	S18E26	12:30	12:50	331×209×174
17	11354	11/11/20-24	118	C6.1	S15E38	16:35 (20)	17:07	218×131×174
18	11358	11/11/25-29	100	C1.1	N19E21	12:02 (26)	12:06	261×174×174
19	11361	11/11/27-04	157	C3.2	N19E26	18:22 (28)	18:39	218×131×174
20	11362	11/11/30-06	154	C4.8	N08W20	16:05 (04)	16:22	261×131×174

Table 2—Continued

NO.	AR	Date	Frames	Maxi ^a Flare	Loc	Begin ^b (UT)	End (UT)	Volume (Mm ³)
21	11363	11/12/02-07	140	C6.9	S20W09	23:20 (05)	23:34	261×174×174
22	11374	11/12/10-13	75	C1.6	S17E43	23:57 (10)	00:07	100×131×174
23	11375	11/12/10-13	80	C1.2	N09E38	06:24 (10)	06:43	200×78×174
24	11381	11/12/19-24	139	C5.4	S19W18	01:56 (22)	02:20	218×113×174
25	11386	11/12/27-31	120	C8.9	S17E32	04:11 (27)	04:31	218×113×174
26	11387	11/12/25-26	48	M4.0	S22W26	18:11 (25)	18:20	158×87×174
27	11389	11/12/31	24	M2.4	S25E44	13:09	13:19	287×244×174
28	11428	12/03/05-11	140	C7.2	S18W03	02:49 (08)	02:56	200×131×174
29	11429	12/03/06-10	114	X5.4	N17E27	00:02 (07)	00:40	218×166×174
30	11430	12/12/05-11	128	X1.3	N22E12	01:05 (07)	01:27	183×131×174
31	11471	12/05/01-07	135	M1.5	S19W44	14:03 (07)	14:52	348×166×174
32	11476	12/05/08-13	132	M4.7	N13E31	12:21 (07)	12:36	305×200×174
33	11494	12/06/04-08	111	M2.1	S19W05	19:54 (06)	20:13	218×122×174
34	11504	12/06/11-17	124	M4.7	S16E18	11:29 (13)	14:31	200×122×174
35	11505	12/06/11-17	111	C1.9	S09E10	00:32 (13)	00:38	131×87×174
36	11512	12/06/26-01	141	C4.2	S16E09	04:45 (28)	04:55	218×131×174
37	11513	12/06/29-04	133	C1.9	N14E04	19:11 (01)	19:21	174×174×174
38	11515	12/06/30-06	153	M6.1	S20W32	11:39 (05)	11:49	261×166×174
39	11520	12/07/11-14	75	X1.4	S19E05	15:373 (12)	17:30	218×218×174
40	11532	12/07/29	7	M2.3	S22E40	06:15	06:29	331×218×174

Table 2—Continued

NO.	AR	Date	Frames	Maxi ^a Flare	Loc	Begin ^b (UT)	End (UT)	Volume (Mm ³)
41	11535	12/08/01-06	125	C3.0	N18E14	21:20 (03)	21:31	218×139×174
42	11542	12/08/09-14	107	C4.2	S16E36	04:07 (10)	04:45	227×157×174
43	11543	12/08/10-16	137	C3.6	N19W36	12:41 (16)	13:48	227×174×174
44	11554	12/08/24-26	74	C1.7	N16E12	02:24 (25)	02:55	200×105×174
45	11560	12/08/30-04	125	C5.5	N07W16	18:00 (02)	18:15	174×131×174
46	11564	12/09/03-08	122	M1.4	S15W36	17:35 (08)	18:20	348×218×174
47	11565	12/09/04-07	65	C2.3	N10E20	07:09 (04)	07:20	145×64×116
48	11569	12/09/13-14	43	C2.6	S13E35	08:23 (13)	08:57	203×93×116
49	11613	12/11/13-19	129	M2.8	S22E33	20:50 (13)	20:57	218×174×174
50	11618	12/11/18-24	132	M3.5	N06E07	15:10 (21)	15:38	261×122×174
51	11620	12/11/24-27	96	M1.0	S14W41	21:05 (27)	21:30	218×113×174
52	11635	12/12/21-28	160	C4.1	N11W14	12:58 (25)	13:07	253×183×174
53	11652	13/01/08-15	138	M1.7	N19W21	08:35 (13)	08:40	305×200×174
54	11654	13/01/11-17	154	M1.0	N06E39	14:51 (11)	15:24	305×209×174
55	11665	13/02/01-05	120	C1.9	N10W04	17:29 (03)	18:32	208×105×174
56	11675	13/02/16-20	64	M1.9	N12E22	15:45 (17)	15:52	121×46×116
57	11692	13/03/13-18	130	M1.1	N11E12	05:46 (15)	08:35	203×151×174
58	11695	13/03/16-18	65	C1.0	N08W04	14:40 (17)	14:56	244×96×174
59	11696	13/03/12-16	108	C2.2	N07W17	10:39 (15)	10:46	244×96×174
60	11718	13/04/06-12	153	M3.3	N19W42	19:52 (12)	20:46	218×122×174

Table 2—Continued

NO.	AR	Date	Frames	Maxi ^a Flare	Loc	Begin ^b (UT)	End (UT)	Volume (Mm ³)
61	11719	13/04/08-14	138	M6.5	N09E12	06:55 (11)	07:29	305×244×174

^aMaxi flare refers to one biggest flare occurring in one AR in the period studied.

^bThe number in parentheses is the date of the flare burst.

^cIt denotes the time.

Table 3: Index α of the frequency-size distributions of FME, FI and magnetic flux.

	FI_{2-day}	FI_{3-day}	E_{3free}	Φ
$FI \geq 0$	$1.6 \pm 0.6(0.90)^a$	$1.4 \pm 0.6(0.99)$	$2.0 \pm 0.4(0.98)$	$1.8 \pm 0.5(0.99)$
$FI_{1-day} \geq 1$	$1.5 \pm 0.5(0.95)$	$1.4 \pm 0.4(0.99)$	$1.9 \pm 0.4(0.98)$	$1.4 \pm 0.5(0.99)$
$FI_{1-day} \geq 10$	$1.5 \pm 0.5(0.95)$	$1.3 \pm 0.4(0.99)$	$1.7 \pm 0.4(0.98)$... ^b
$FI_{2-day} \geq 1$	$1.5 \pm 0.6(0.90)$	$1.4 \pm 0.4(0.99)$	$1.9 \pm 0.4(0.98)$	$1.5 \pm 0.6(0.99)$
$FI_{2-day} \geq 10$	$1.5 \pm 0.6(0.90)$	$1.5 \pm 0.4(0.99)$	$1.8 \pm 0.4(0.95)$	$0.8 \pm 0.5(0.99)$
$FI_{2-day} \geq 50$	$1.5 \pm 0.9(0.75)$	$1.4 \pm 0.6(0.99)$	$1.5 \pm 0.5(0.98)$	$1.2 \pm 0.6(0.99)$
$FI_{3-day} \geq 1$	$1.5 \pm 0.6(0.90)$	$1.4 \pm 0.4(0.99)$	$1.9 \pm 0.4(0.98)$	$1.9 \pm 0.6(0.99)$
$FI_{3-day} \geq 10$	$1.5 \pm 0.6(0.90)$	$1.4 \pm 0.4(0.99)$	$1.8 \pm 0.4(0.98)$	$1.0 \pm 0.5(0.99)$
$FI_{3-day} \geq 50$	$1.5 \pm 0.6(0.90)$	$1.4 \pm 0.6(0.99)$	$1.6 \pm 0.5(0.98)$	$1.3 \pm 0.5(0.98)$

^aThe number in parentheses is the significance level of χ^2 -test.

^bThe value is not shown as it is much less than the error. Likewise, when the threshold is set as $FI \geq 50$ in the time window $\tau = 1$ day, the values of α do not make sense and are not shown.

Table 4. Flare productivity for $E_{3free} = 5 \times 10^{32}$ ergs or $\sim \Phi = 3 \times 10^{22}$ Mx under different threshold of FI and different time window of τ -days.

FI	$\tau = 1\text{-day}$		$\tau = 2\text{-days}$		$\tau = 3\text{-days}$	
	E_{3free}	Φ	E_{3free}	Φ	E_{3free}	Φ
≥ 1 (C1.0)	0.95	0.85	0.98	0.93	1.00	0.95
≥ 10 (M1.0)	0.70	0.45	0.90	0.70	0.95	0.80
≥ 50 (M5.0)	0.28	0.15	0.45	0.40	0.50	0.45
≥ 100 (X1.0)	0.20	0.10	0.30	0.15	0.32	0.32

Table 5: Correlations of the magnetic measures with FI/Φ for all the data ($FI \geq 0$).

	$FI_{1\text{-day}}$	$FI_{2\text{-day}}$	$FI_{3\text{-day}}$	Φ
E_{3free}	0.53 (100%) ^a	0.57 (100%)	0.58 (100%)	0.91 (100%)
Φ	0.50 (100%)	0.55 (100%)	0.57 (100%)	1.00 (100%)
I_t	0.53 (100%)	0.59 (100%)	0.60 (100%)	0.98 (100%)
E_{pe}	0.59 (100%)	0.64 (100%)	0.65 (100%)	0.96 (100%)
α_{av}	0.42 (100%)	0.42 (100%)	0.42 (100%)	0.23 (100%)

^aThe number in parentheses is the Spearman rank correlation’s confidence level.

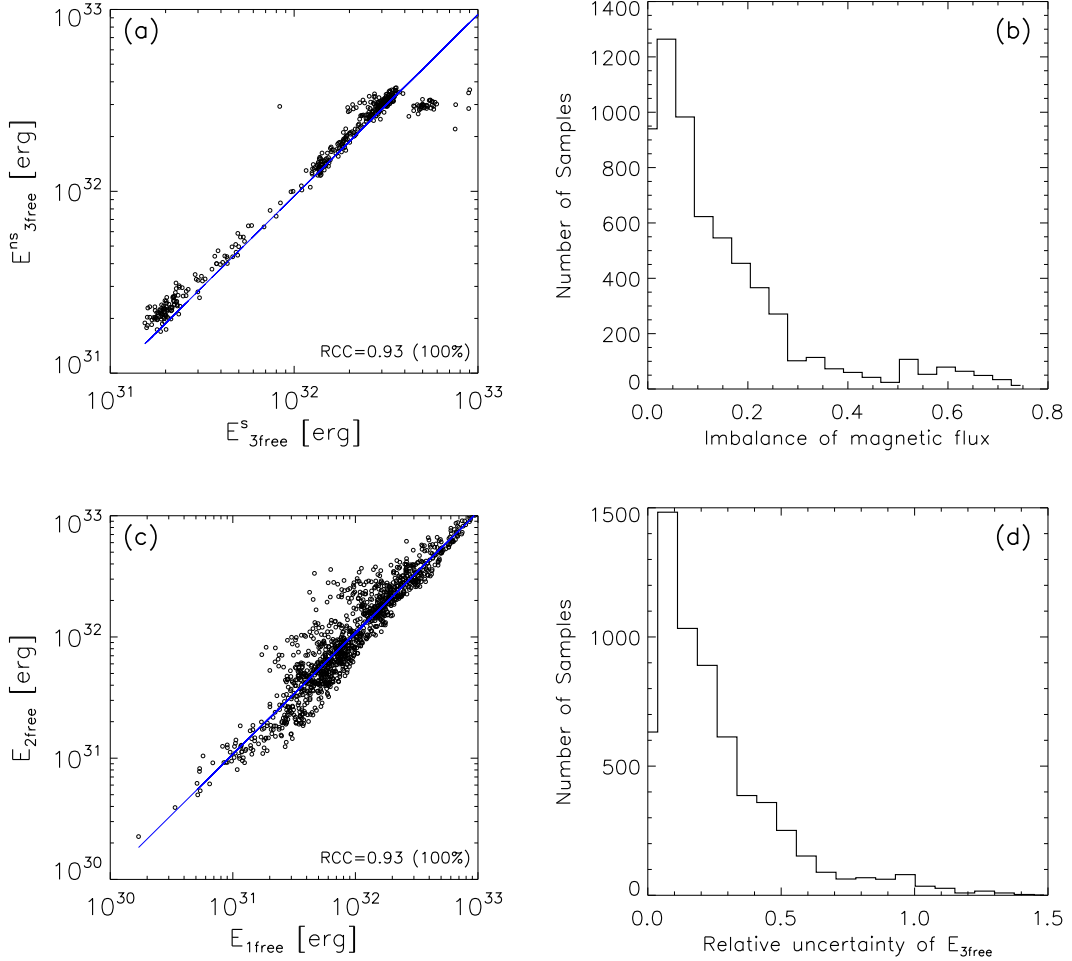


Fig. 1.— Assessment of the quantities related to the uncertainty of the determined FMEs. Panel (a) corresponds to a data sample of NOAA AR 11158 alone, while panels (b-d) correspond to the entire data sample. (a) E_{3free}^s vs. E_{3free}^{ns} , obtained from the testing vector magnetograms being smoothed and not smoothed, respectively. (b) Histogram of the relative imbalance of magnetic flux. (c) E_{1free} vs. E_{2free} . (d) Histogram of the relative uncertainty of E_{3free} . The blue lines are linear fittings to the data.

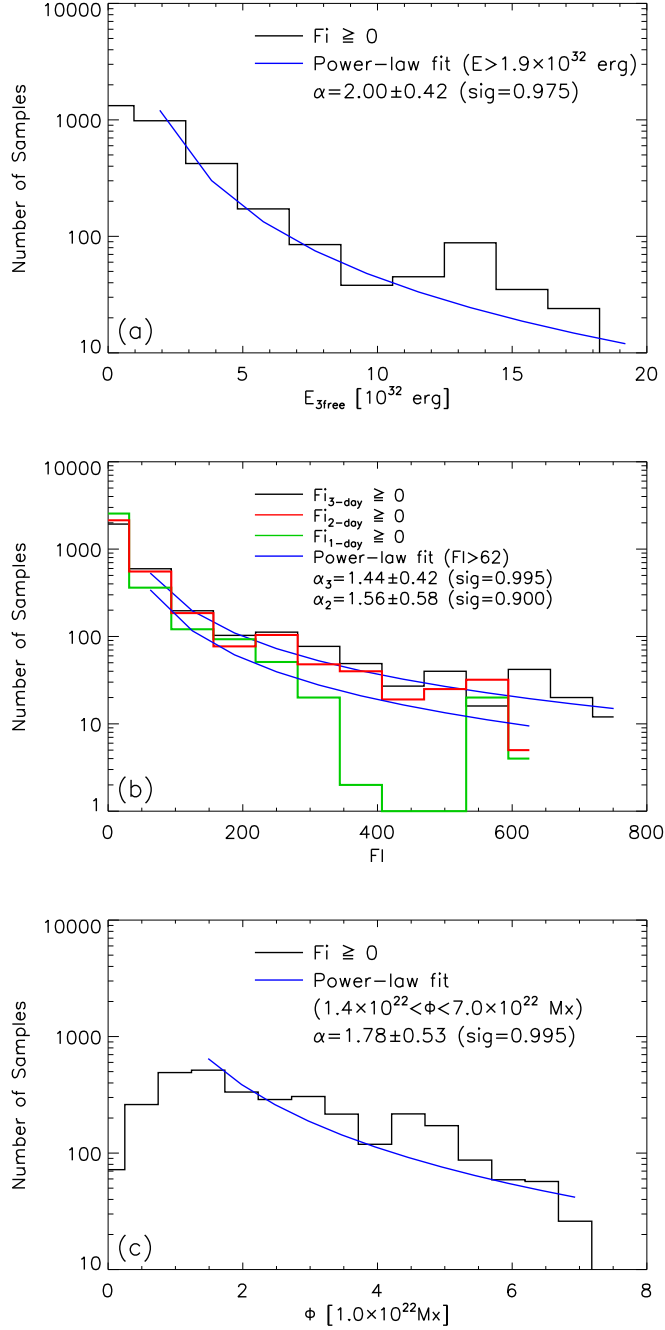


Fig. 2.— Histograms of FME (a), FI (b) and magnetic flux (c) of all the data ($FI \geq 0$). The blue lines are the nonlinear fittings to the histograms (black or red) created in the χ^2 -test. In panel (b), the FI for $\tau = 1$ -day window was not fitted due to insufficient data when $FI > 350$ (the sample size $N < 5$). Likewise, the data in panel (c) was not fitted when $\Phi > 7 \times 10^{22} \text{ Mx}$. The lower-cutoff and the significance level are marked in parentheses.

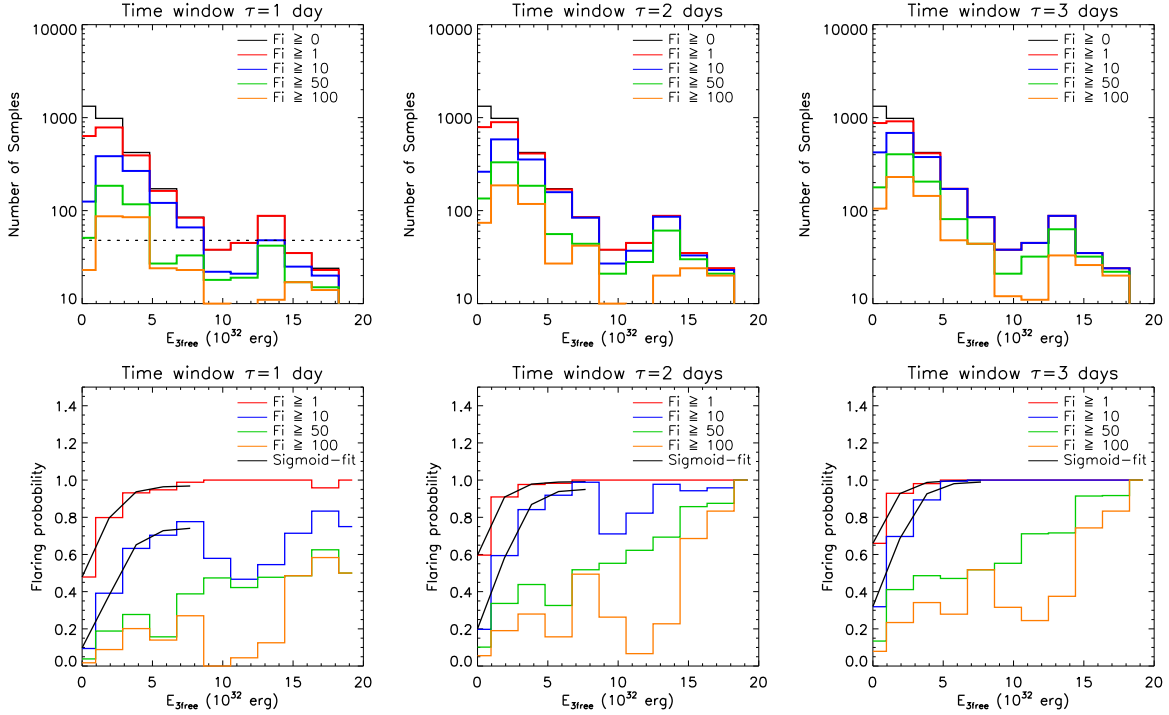


Fig. 3.— Histograms of E_{3free} (top panels) and flare productivity P (bottom panels) predicted with the measurements in the time windows of $\tau = 1 - 3$ days for different thresholds of FI (indicated by black, red, blue, green and yellow colors). The solid black lines in the bottom panels are the sigmoid function fittings to the flare productivity with the sample size $N > 50$.

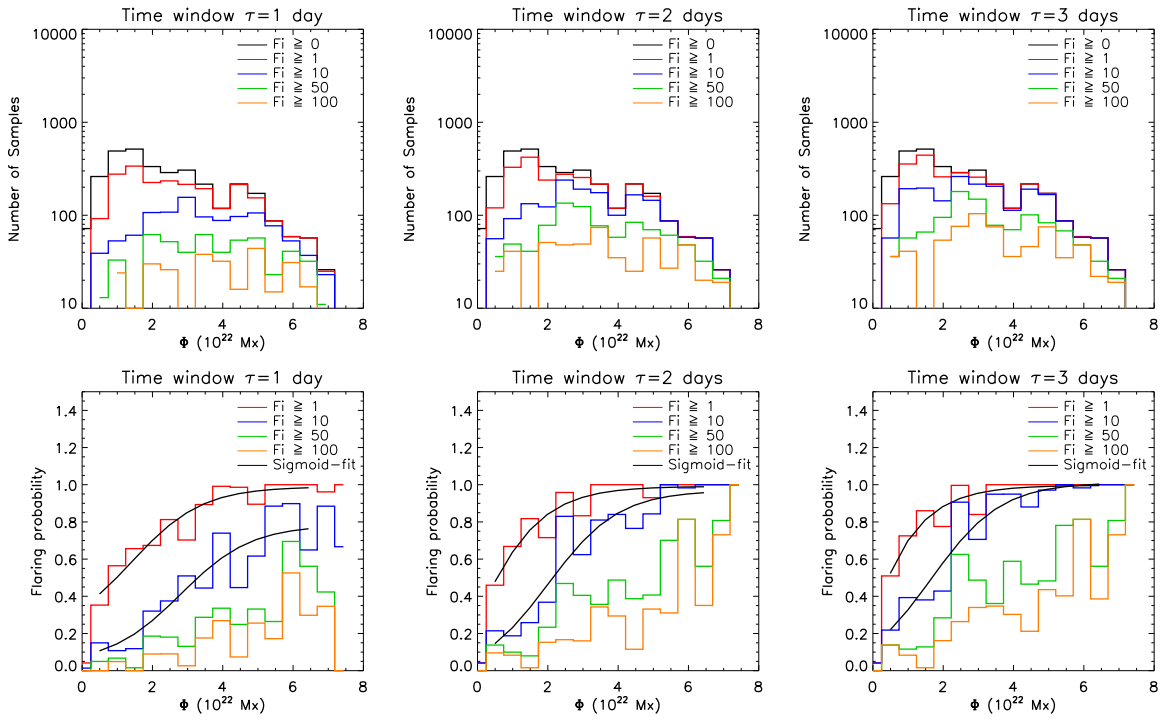


Fig. 4.— Same as Figure 3, but for the measure of Φ .

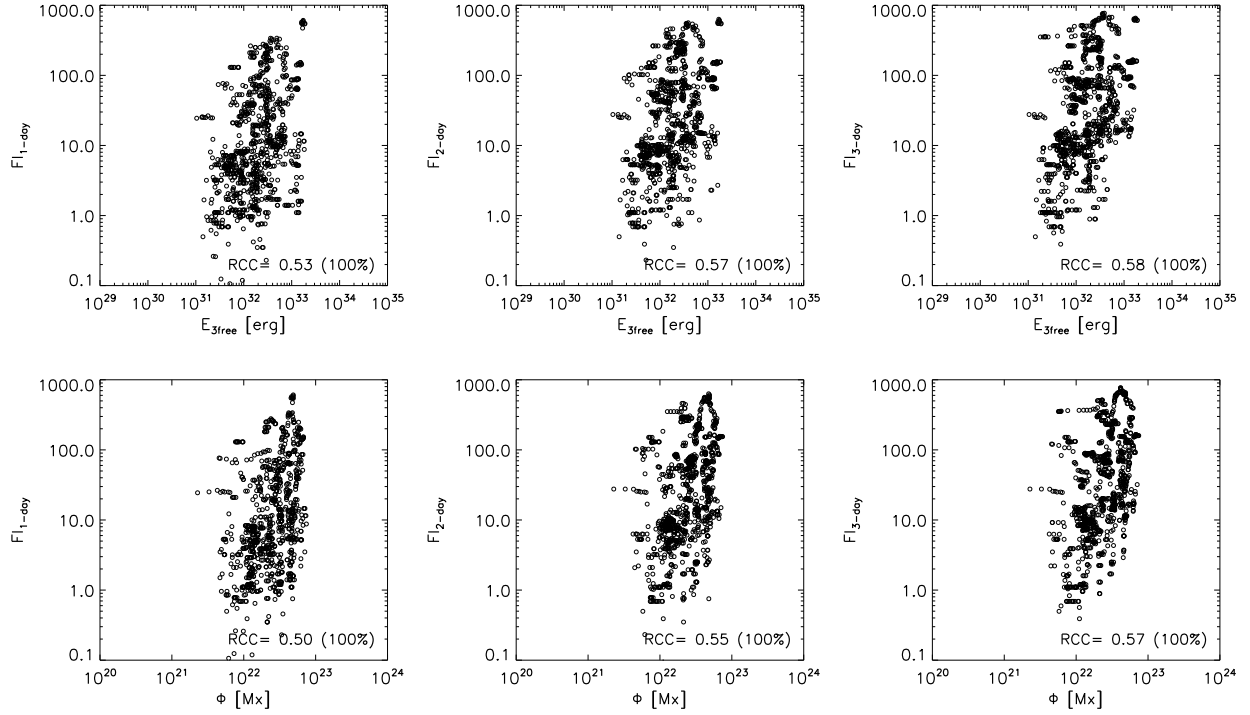


Fig. 5.— Scatter plots of the FI versus the magnetic measures E_{3free} (top panels) and Φ (bottom panels). Shown from left to right are the panels in the time windows of $\tau = 1 - 3$ days, respectively. The number in the bottom right corner of each panel is the Spearman rank-correlation coefficient and that in parentheses is the correlation’s confidence level in percent.

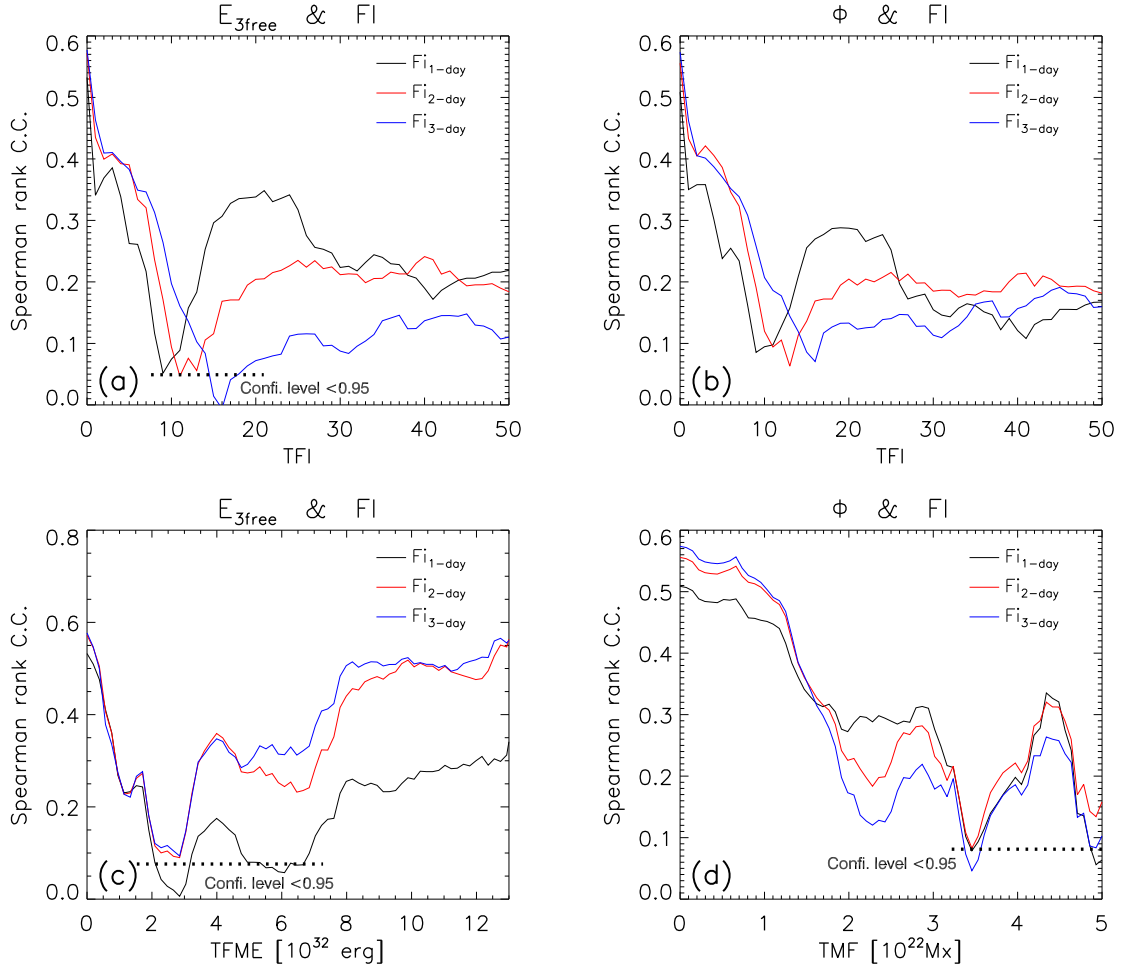


Fig. 6.— Correlation varying with the threshold of the parameters, FI , FME and Φ . The RCC between $E_{3\text{free}}$ and FI versus TFI is shown in (a), and that versus $TFME$ in (c). The RCC between Φ and FI versus TFI is shown in (b), and that versus TMF in (d). The curves in the time windows of $\tau = 1 - 3$ days are illustrated by black, red and blue colors, respectively. The data below the dotted-lines have confidence level < 0.95 .

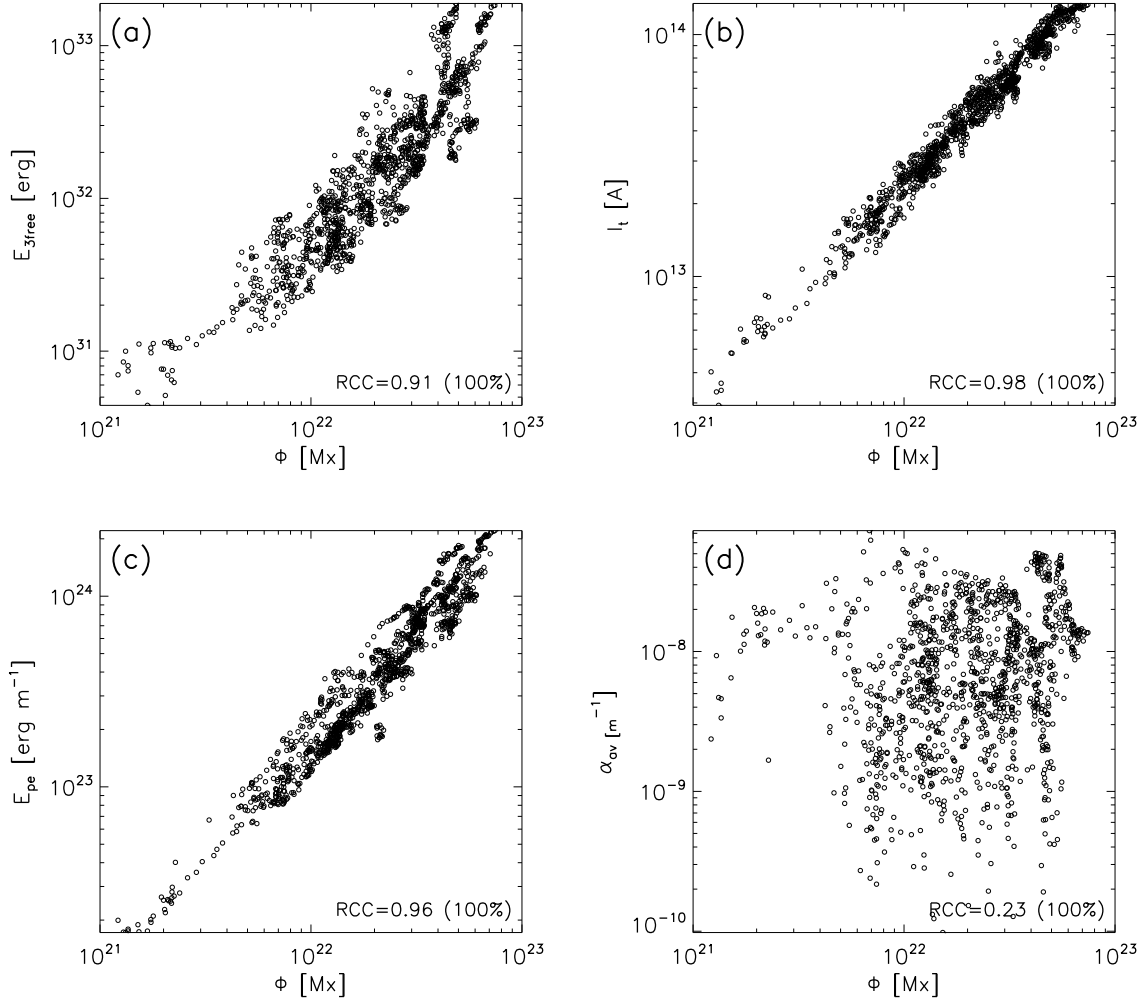


Fig. 7.— Scatter plots of Φ vs. E_{3free} (a), I_t (b), E_{pe} (c) and α_{av} (d). The number in the bottom right corner of each panel is the Spearman rank-correlation coefficient and that in parentheses is the correlation’s confidence level in percentage.